UC Santa Barbara
UC Santa Barbara Previously Published Works

Title

Nanoscale Iron Nitride, e-Fe$_3$N: Preparation from Liquid Ammonia and Magnetic Properties

Permalink

https://escholarship.org/uc/item/9k10b1xq

Journal

Chemistry of Materials, 29(2)

ISSN

0897-4756 1520-5002

Authors

Zieschang, Anne-Marie
Bocarsly, Joshua D
Dürrschnabel, Michael
et al.

Publication Date

2017-01-24

DOI

10.1021/acs.chemmater.6b04088

Peer reviewed

Nanoscale Iron Nitride, ε-Fe₃N: Preparation from Liquid Ammonia and Magnetic Properties

Anne-Marie Zieschang,[1] Joshua D. Bocarsly,[2] Michael Dürrschnabel,[3] Leopoldo Molina-Luna,[3] Hans-Joachim Kleebe,[3] Ram Seshadri,*[2] Barbara Albert*[1]

[1]Technische Universität Darmstadt, Eduard-Zintl-Institute of Inorganic and Physical Chemistry, Alarich-Weiss-Str. 12, 64287 Darmstadt, Germany

[2] University of California, Santa Barbara, Department of Chemistry & Biochemistry, Materials Department, and Materials Research Laboratory, University of California, Santa Barbara CA 93106, U.S.A.

[3]Technische Universität Darmstadt, Department of Materials and Geosciences, Alarich-Weiss-Str. 2, 64287 Darmstadt, Germany

ABSTRACT: ε-Fe₃N shows interesting magnetism but is difficult to obtain as a pure and single-phase sample. We report a new preparation method using the reduction of iron(II) bromide with elemental sodium in liquid ammonia at –78 °C, followed by annealing at 573 K. Nanostructured and monophasic oxygen-free iron nitride, ε-Fe₃N, is produced according to X-ray diffraction and transmission electron microscopy experiments. The magnetic properties between 2 K and 625 K were characterized using a vibrating sample magnetometer, revealing soft ferromagnetic behavior with a low-temperature average moment of 1.5 μ_B/Fe and a Curie temperature of 500 K. T_C is lower than that of bulk ε-Fe₃N (575 K),[1] which corresponds well with the small particle size within the agglomerates (15.4 (± 4.1) nm according to TEM, 15.8(1) according to XRD). Samples were analyzed before and after partial oxidation (Fe₃N-Fe$_x$O$_y$ core-shell nanoparticles with a 2–3 nm thick shell) by X-ray diffraction, transmission electron microscopy, electron energy-loss spectroscopy and magnetic measurements. Both the pristine Fe₃N nanoparticles and the oxidized core-shell particles showed shifting and broadening of the magnetic hysteresis loops upon cooling in a magnetic field.

Introduction

Iron nitrides show exceptional physical properties[2-5] that can be used for various applications such as magnetic recording media,[5,6] catalysis,[7] and biomedical applications.[8] They are cheap and exhibit high saturation magnetization and very high magnetic moments.[4,6] The investigation of their interesting magnetism is hindered by the difficulty to prepare magnetically pure phases in sufficiently large quantities. A recent review discusses the synthesis and properties of iron nitrides at reduced dimensions.[9] Many iron nitrides show ferromagnetic behavior. The most important ferromagnetic iron nitrides are α''-$Fe_{16}N_2$, ϵ-Fe_3N_{1+x} and γ'-Fe_4N. Concerning their structures, all of the iron nitrides can be thought of as iron in an ordered or distorted hcp (ϵ, Figure 1), bcc (α) or fcc (γ) structure with interstitial nitrogen atoms. Thus, ϵ-Fe_3N and ϵ-Fe_2N can be considered boundary compositions of a single phase with a broad homogeneity range, ϵ-Fe_3N_{1+x}. Depending on the nitrogen content and crystal structure the magnetic moment of the ferromagnetic iron nitrides varies from up to 3.0 μ_B/Fe for α''-$Fe_{16}N_2$[4] to 1.8 μ_B/Fe for Fe_3N.[10]
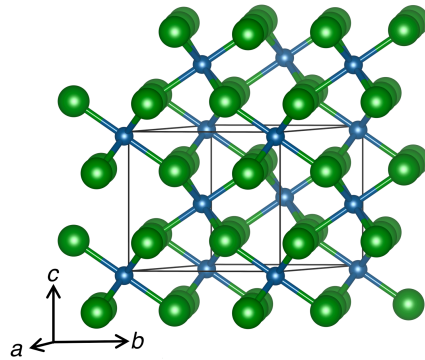

Figure 1: Structure of ϵ-Fe_3N with blue nitrogen atoms and green iron atoms. Nitrogen interstitials are located in the octahedral sites of a hexagonally closed packed iron lattice.

The most common synthesis route for iron nitride nanoparticles is nitridation of nanoparticles of elemental iron, iron oxides or hydroxides using ammonia gas.[9,11] Physical methods such as reactive sputtering lead to thin films.[12,13] Liquid ammonia is an exotic but versatile solvent that can be used in organic and inorganic reactions.[14-16] Its ability to dissolve alkaline and alkaline earth metals makes it especially interesting for reduction reactions.[16] Solutions of alkaline metals have been used by Watt et al. to react various transition metal salts and oxides.[17-20] After reducing iron(II) bromide with an excess of potassium in liquid ammonia they described the formation of Fe_3N. Recently, this solvent was used to produce nanoparticles of several transition metals (e.g. Bi, Re, Co, W)[21-23] and metal nitrides (e.g.CoN, GaN).[21] The reduction of titanium salts using a solution of sodium in liquid ammonia to produce titanium nitride nanoparticles has been shown.[24]

Now, nanoscale and pure ϵ-Fe_3N was obtained by annealing a precipitate obtained from $FeBr_2$ and sodium in liquid ammonia. The samples proved to be single-phase according to X-ray diffraction (XRD) and transmission electron microscopy (TEM), and ignite immediately when brought into air. They were magnetically characterized, and we present a rare example of a high-temperature magnetic study on iron nitrides. Furthermore, in a separate experiment the iron nitride was slightly oxidized to produce Fe_3N-Fe_xO_y core-shell particles. Such composites between different magnetic substances of varying hardness are interesting for tuning the properties of magnetic materials.[25]

Experimental Section

Synthesis. All glassware was heated *in vacuo* and then flushed with argon three times to remove all traces of water and oxygen. Prior to the synthesis, ammonia (Air Liquide, UHP, < 5 ppm H_2O) was condensed into a cooling trap at −78 °C and dried with sodium for 24 h. $FeBr_2$ (Sigma-Aldrich, 98 %) was stored in a glove box and used without further purification. The nanoparticles were produced in a three-neck flask by adding 1.05 equivalents of sodium to a suspension of $FeBr_2$ in about 50 ml of liquid ammonia. The reaction temperature was kept at −78 °C for two hours. During that time the flask was taken out of the cold bath to be stirred for one minute every 20 minutes. After the reaction, the mixture was allowed to warm to room temperature. When all ammonia had evaporated, the powders (sample size about 2 g) were dried *in vacuo* for eight hours, annealed at different temperatures (temperature program in SI), and then washed with methanol. They were transferred into the measurement devices (XRD, VSM, TEM) without exposure to air. To allow for partial oxidation and production of core-shell particles selected samples were reacted with an air/nitrogen or air/argon mixture for ten minutes at room temperature before transferring them into the magnetometer or transmission electron microscope.

Structural characterization. X-ray powder diffraction data was collected at room temperature by a powder diffractometer (STOE Stadi P, position-sensitive detector) with $MoK_{α1}$ radiation (Ge(111) monochromator, $λ = 0.70930$ Å, glass capillary, Debye-Scherrer geometry, position-sensitive detector). Particle size determination was performed using the Scherrer formula (program TOPAS).[32]

Magnetic properties were measured in a Quantum Design Physical Property Measurement System (PPMS DynaCool) outfitted with a vibrating sample magnetometer (VSM) with a high-temperature oven option (QD VSM and QD VSM oven). Measurements between 2 K and 400 K were carried out by loading a known mass (5–10 mg) of nanopowder particles into a polypropylene capsule, sealing the seam with vacuum grease to prevent any air contact, and then quickly transferring the capsule into the magnetometer (He or vacuum environment). Measurements between 300 K and 625 K were taken by loading powder into a small piece of silver tube in a glovebox, and tightly crimping each end of the tube to make an air-tight packet. The packet was then removed from the glovebox, cemented onto a heater stick and placed into the VSM. For this high-temperature measurement, we were not able to accurately weigh the powder, so we determined the mass by comparing the room-temperature saturation magnetization of the nanoparticles in the silver tube to the room-temperature saturation magnetization of the weighed sample in the polypropylene capsule.

Transmission electron microscopy. A 200 kV JEOL JEM 2100F (scanning) transmission electron microscope (STEM) equipped with an Oxford X-Max80 detector was used to determine the microstructure and identify the phases on the nanometer scale. Quantitative energy-dispersive X-ray spectroscopy (EDS) analysis was carried out using the Cliff-Lorimer k-factor method. A Gatan transfer specimen holder model 648 was used to protect the samples from oxidation. The evaluation of diffraction data was carried out using the DiffTools script.[26] The JEMS software[27] was used to simulate powder diffraction pattern and high resolution phase contrast thickness-defocus maps using 200 keV electrons for Fe_3N (ICSD No. 33576).[28] Grain sizes of 2 nm and 10 nm were used for the sample before and after annealing, respectively. The parametrization of Peng, Ren, Dudarev, and Whelan was used to calculate the atomic form factors[29] needed for calculating the powder diffraction data.

For electron energy-loss spectroscopy (EELS) experiments in combination with scanning transmission electron microscopy an aberration-corrected JEOL JEM ARM-F microscope was used. The microscope was operated at 120 kV to reduce beam damage and to enhance the cross-section for EELS. It is equipped with a "Schottky" field-emission gun (FEG) and a Gatan Enfina EEL spectrometer. The energy-resolution in EELS, as measured by the full-width half-maximum of the zero-loss peak, was about 0.8 eV. At the microscope settings used, the electron probe size for the

EELS was less than 1 nm. A 50 μm condenser aperture was used corresponding to a convergence angle α = 42.2 mrad. A camera length of 6 cm and a spectrometer entrance aperture of 3 mm were used corresponding to a collection angle β of 7 mrad. The corresponding high-angle angular dark-field (HAADF) detector angles were 90-370 mrad. EEL spectra were recorded with a dispersion of 0.3 eV/channel and a spectrometer entrance aperture of 3 mm, which allowed to simultaneously acquire the N-K, O-K and Fe-$L_{2,3}$ ionization edges. A power law function and the Hartree-Slater model were used to remove the background and to quantify the composition. The integration widths for the quantification were $401.0 - 426.2$ eV for the N-K edge, $532.0 - 572.0$ eV for the O-K, and $708.0 - 748.0$ eV for the Fe-$L_{2,3}$ edge. Spatially resolved STEM-EELS maps were acquired using the following settings: 12 x 14 pixels (15 x 17 nm), 5 s acquisition time per pixel, and 0.3 eV energy dispersion. The EELS data cube was filtered using principal component analysis (PCA)[30] with ten components to reduce the contribution of noise on the EELS signal.[31]

Results and discussion

Reduction of $FeBr_2$ in liquid ammonia and subsequent annealing resulted in products (Fe-N) with varying nitrogen content, depending on the annealing temperature. Temperatures of 573 K led to single-phase ε-Fe_3N according to XRD with an average particle size of 15.8(1) nm and 15.4 (± 4.1) nm (58 particles) determined from the TEM bright-field image shown in Figure 2 (a) (see also SI). The agglomeration of particles could not be avoided since the particles are ferromagnetic. The high-resolution phase contrast image (Figure 2 (b) indicates good crystallinity of the nanoparticles. A phase contrast image simulation under Scherzer focus condition and assuming a sample thickness of 6.4 nm is shown in Figure 2 (b, white rectangle) to emphasize its stability. The contrast can then be interpreted the following way: the dark spots correspond to nitrogen dumbbells surrounded by iron dumbbells. The inset on the lower right shows the corresponding diffractogram, which was indexed using the structure of ε-Fe_3N. Figure 2 (c) shows a selected area electron diffraction pattern acquired from the area indicated in Figure 2 (a). The indexing was carried out using the ε-Fe_3N structure model from literature.[28] Comparing this diffraction pattern with Figure 6 (c) it is evident that the crystallinity is higher for Fe_3N compared to Fe_2N (obtained at 473 K), since no amorphous ring-type overlay was found. A radial intensity profile (Figure 2 (d)) was extracted from the electron diffraction pattern (Figure 2 (c)) via rotational averaging and compared to simulated powder diffraction patterns of the ε-Fe_3N phase. It indicates that the nanoparticles are indeed single phase ε-Fe_3N with a structure matching the XRD observations.
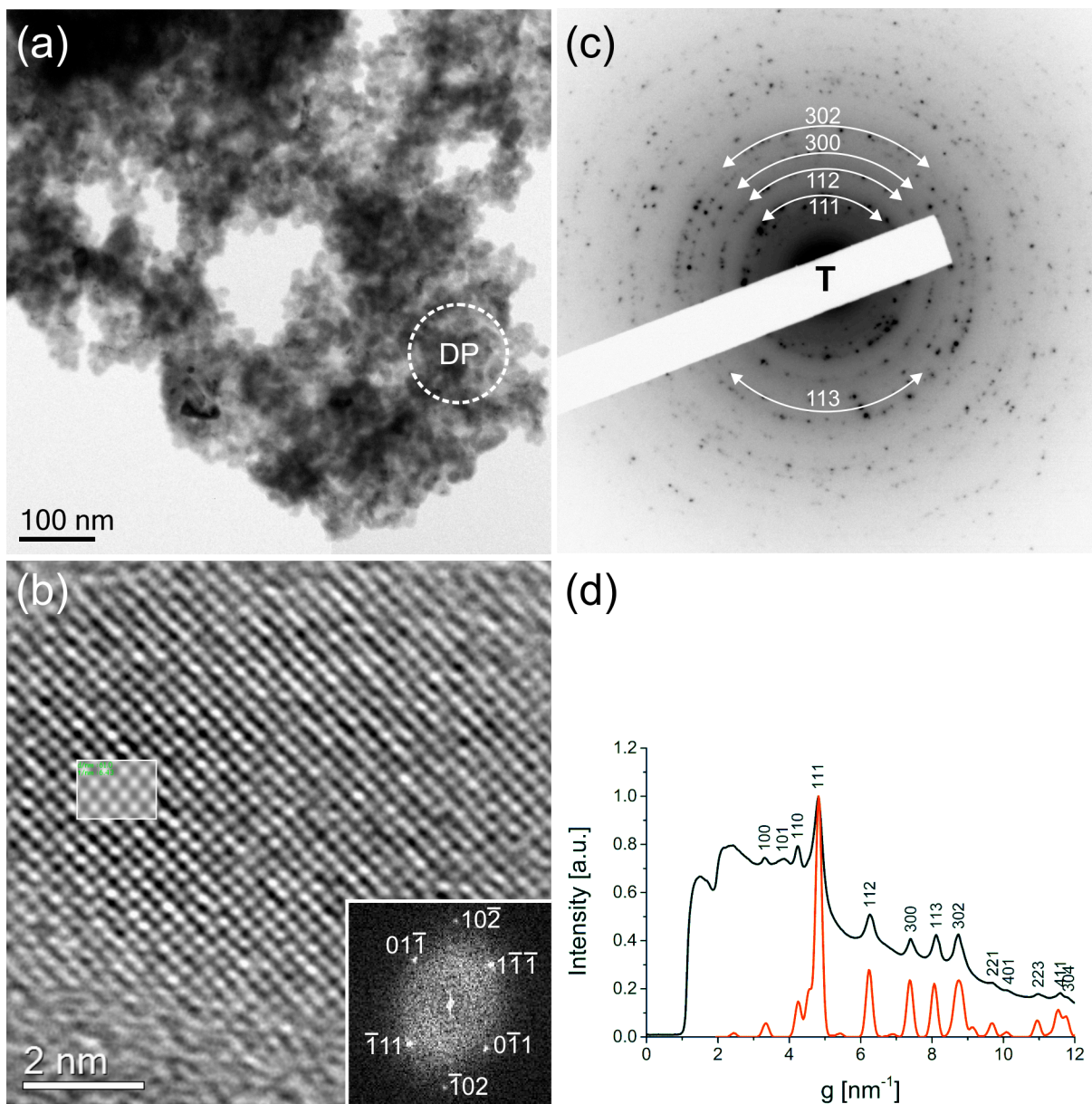
Figure 2: (a) Bright-field diffraction contrast TEM image of an agglomerate of Fe_3N nanoparticles annealed at 573 K. (b) High-resolution phase contrast image of a crystalline iron nitride nanoparticle in [211] zone axis orientation. The inset on the lower right shows the indexed Fast Fourier Transform, whereas the other inset shows a high resolution phase contrast image simulation of Fe_3N. (c) Selected area electron diffraction pattern of the region marked in (a) with Fe_3N indices. (d) Radial intensity profile overlaid by simulated powder diffraction plot of Fe_3N.

The nanoparticles of Fe_3N show soft ferromagnetic behavior and a saturated average magnetic moment of 1.5 μ_B/Fe (M_S = 144 emu/g) at 2 K (Figure 3). This behavior is consistent with reports of magnetism in bulk ε-Fe_3N, which has been reported to have a moment of 1.3 μ_B/Fe to 2.0 μ_B/Fe from magnetization and neutron diffraction studies[33,34] and 1.6 μ_B/Fe to 2.25 μ_B/Fe from density functional theory calculations.[35-37] Even more variability is reported for thin films, nanowires, and nanoparticles, with saturation magnetizations ranging from 0.16 μ_B/Fe to 1.4 μ_B/Fe.[9,38] The high saturation magnetization of the samples reported here, as well as the shape of the magnetic hysteresis loops, further supports the TEM and XRD evidence that the particles are high quality ε-Fe_3N. The samples show onset of ferromagnetism at T_C = 500 K (Figure 3 (a)), slightly lower than the reported Curie temperature of bulk ε-Fe_3N, T_C = 575 K.[34] This lowering of T_C is commonly observed in ferromagnetic nanoparticles, and can be interpreted as weakened exchange interactions due to disorder at the nanoparticle surface. The magnetization as a function of temperature at low field (H = 200 Oe) shows a difference between the zero field cooled (ZFC) and field cooled (FC) magnetization, with a maximum in the ZFC (blocking temperature) of 410 K.

Figure 3 (b) shows magnetization as a function of field $M(H)$ for the ε-Fe_3N. At low temperature, some hysteresis is observed, while the sample is very magnetically soft at room temperature. At temperatures well above the Curie temperature, linear dependence of magnetization on field is expected. Because the iron nitride particles degrade at elevated temperatures, no measurements above 625 K could be obtained. Consequently, this linear $M(H)$ was not observed. It is therefore difficult to determine whether any ferromagnetic impurities (*e.g.* α-Fe or α''-$Fe_{16}N_2$) with high Curie temperatures are present in the ε-Fe_3N. However, by comparing the remnant magnetism of the sample at 625 K to the moment of iron at the same temperature,[39] it can be determined that, if there is an α-Fe impurity, it comprises less than 5% of the sample by mass.
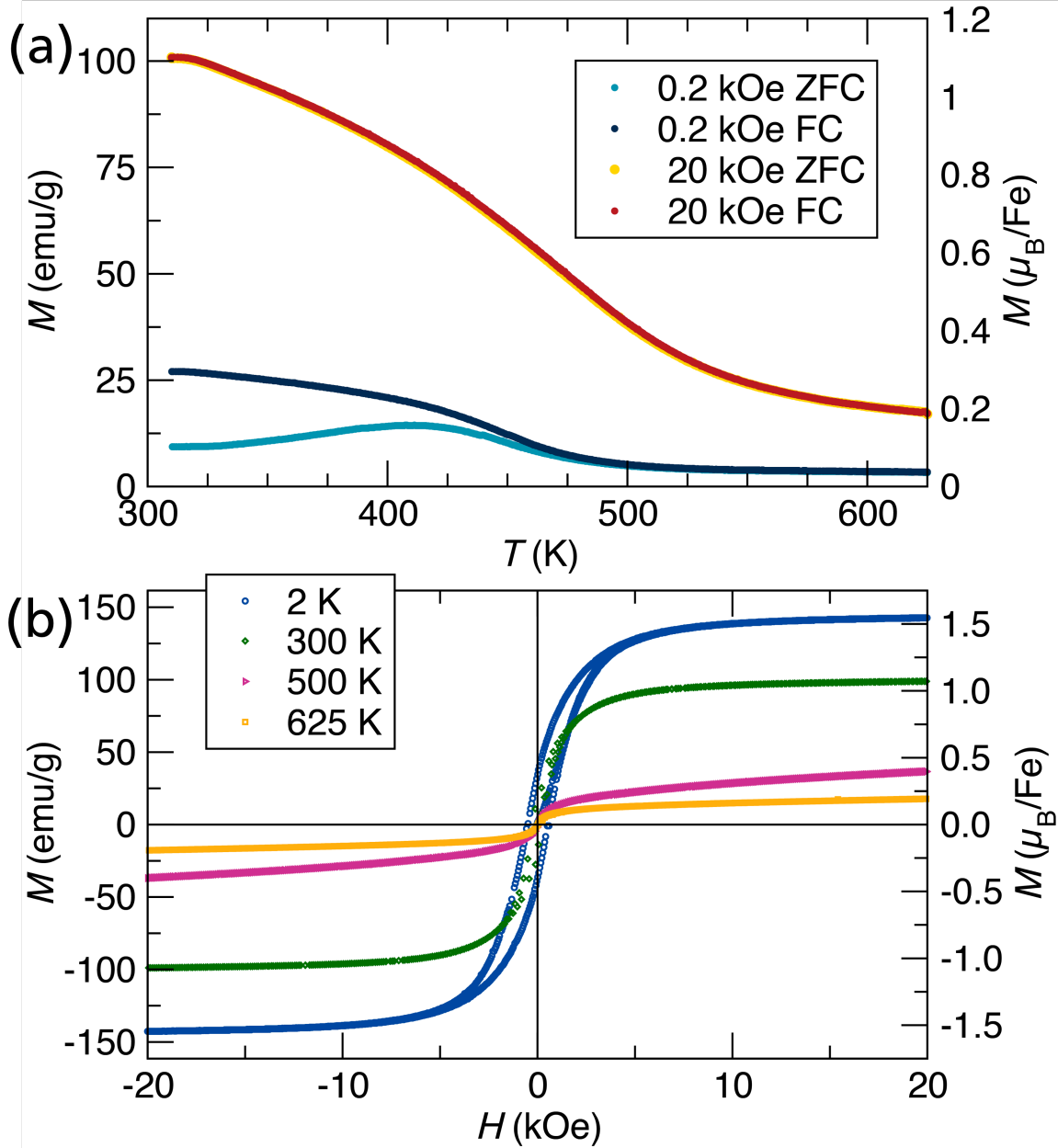
Figure 3: *M(T)* and *M(H)* measurements of Fe₃N nanoparticles. (a) shows the zero field cooled (ZFC) and field cooled (FC) isofield magnetization at two different applied fields, demonstrating onset of ferromagnetism at 500 K and a blocking temperature of 410 K. The ZFC and FC curves at $H = 2$ T are overlapping. (b) The isothermal magnetization at several temperatures. The particles show soft ferromagnetic behavior, with a coercivity of 490 Oe and a saturation moment of 1.5 μ_B/Fe at 2 K. The saturated moment and coercivity decrease with increasing temperature.

When samples were brought into air quickly, the powders proved to be highly pyrophoric. The color of the powder changed from black to orange immediately. However, exposing the powders to air slowly (as described in the experimental section) seemed to stabilize them towards oxidation. Thus, in a separate experiment, selected Fe₃N samples were partially oxidized to produce core-shell nanoparticles and then analyzed using STEM-EELS. Figure 4 shows a bright-field STEM image (a) and a STEM-HAADF image of a single iron nitride/iron oxide core-shell nanoparticle. The shell thickness was determined from the image to be 2.5 nm. To ensure that an iron oxide shell is observed around the nanoparticle, a 2D STEM-EELS map was acquired from a second particle. The elemental maps were extracted from the EELS data cube, which was corrected for background and filtered by principal component analysis to reduce the noise for N-K, O-K, and Fe-L₂,₃ edge, respectively. The result for each element is shown in false

colors in Figure 4 (c-e). The RGB map shown in Figure 4 (f) was created from the single elemental maps (Figure 4 (c-e)) by assigning N-K a red color, Fe-$L_{2,3}$ a green color, and O-K a blue color. The oxide shell is directly visible by the blue color surrounding the yellowish nanoparticle core. Figure 4 (g) shows single EEL spectra extracted from representative core (red curve) and the shell (black curve) regions. The nanoparticle core exhibits a clear nitrogen edge, whereas the N-K edge was not observed in the shell indicating an iron nitride/iron oxide core-shell structure of the nanoparticle. In Figure 4 (h) the EEL spectrum of the shell from Figure 4 (g) (black curve) is compared via the energy-loss near edge-fine structure (ELNES) to an EEL reference spectrum (red curve).[40] The reference spectrum (Fe_2O_3, α or γ was not specified) shows a different peak setup of the O-K ELNES compared to our measurement indicating a different iron oxide phase in our case. A review of EELS analyses of the different iron oxide phases can be found in the work of Colliex et al.[41] or Calvert et al.[42] If we qualitatively compare the O-K ELNES of our EELS measurement with the results from literature we find that our O-K ELNES matches best with the O-K ELNES of iron monoxide, $Fe_{1-x}O$. This finding is supported by the quantification of our EEL spectrum yielding an oxygen to iron ratio of 1:1 (50.40 at% : 49.60 at%). On the other hand, if the Fe_2O_3 reference spectrum from ref. 40 is quantified, an oxygen to iron ratio of 3:2 is obtained (62.38 at% : 37.62 at%). The X-ray diffraction data of Fe_3N after exposure to air did not show any reflections of iron oxides.
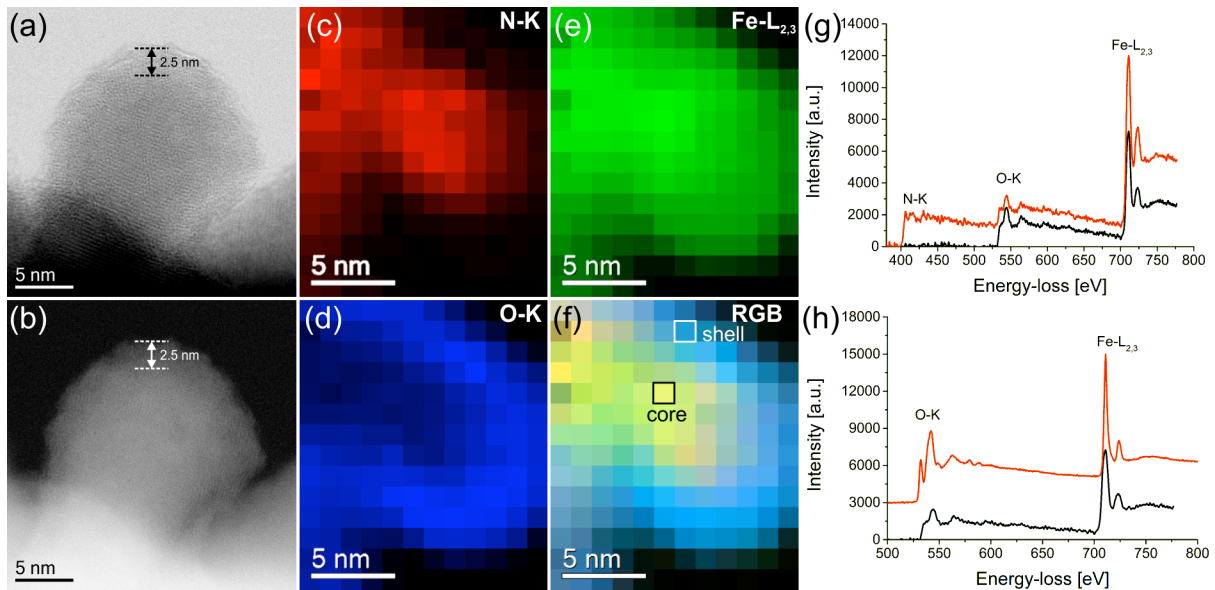

Figure 4: (a) Bright-field STEM image and (b) STEM-HAADF image of a Fe_3N/FeO core-shell nanoparticle. STEM-EELS elemental maps of a different nanoparticle are shown in false color using the N-K (c), O-K (d) and Fe-$L_{2,3}$ (e) ionization edges. (f) RGB map (red: N-K, green: Fe-$L_{2,3}$, blue: O-K) is shown. (g) Comparison of an EEL spectrum extracted from representative core region (red curve) and a shell region (black curve) as indicated in the RGB map. (h) Comparison of the ELNES of the particle shell (black curve) with literature data (red curve).[40]

As shown in Figure 5, the oxidized nanoparticles have a smaller saturation magnetization than the pristine particles (144 emu/g *vs*. 112 emu/g at 2 K), suggesting that, as expected, the oxidized surface has lower magnetization than the clean nitride surface. Field-cooling the Fe_3N nanoparticles leads to a shifting and broadening of the hysteresis loops, both for the pristine, unoxidized Fe_3N nanoparticles and for oxidized core-shell particles. This behavior has previously been observed in Fe_3N particles with Fe_3O_4 on the surface.[43] Such asymmetry of the hysteresis loop upon field cooling is typical of exchange bias hardened systems, where a ferromagnetic phase has an interface with an antiferromagnetic phase. When such a sample is cooled under a large magnetic field, all of the antiferromagnetic surfaces will become polarized in one direction to minimize exchange energy with the polarized ferromagnetic phase. Then, exchange

interactions with the polarized antiferromagnetic surfaces "pin" the polarization of the ferromagnet, and an increased coercive field is required to flip its direction from the direction of field-cooling. Such exchange bias behavior may be expected in core-shell structured nanoparticles where one phase is ferromagnetic and the other is antiferromagnetic, as is likely the case for Fe–N/Fe–O core-shell particles, and this mechanism was used to explain the shifted hysteresis loops previously reported in the Fe_3N/Fe_3O_4 particles.[44] However, the oxygen-free nanoparticles synthesized in this study show nearly as much shifting of the hysteresis loop as the oxidized samples ($H_E = 220$ Oe for the pure particles and $H_E = 300$ Oe for the oxidized core-shell particles). This indicates that the exchange bias-like behavior cannot be attributed principally to the nitride-oxide core-shell structure.

Exchange bias-like behavior is also observed in single phase systems with glassiness or competing exchange interactions.[45,46] The present results indicate that the shifting of the hysteresis loops in both the pristine and oxidized samples are likely driven by mixed exchange interactions in the Fe–N caused by disorder at the nanoparticle surfaces. This mechanism is consistent with the observed spin-glass behavior in iron nitride nanoparticles.[9,44]
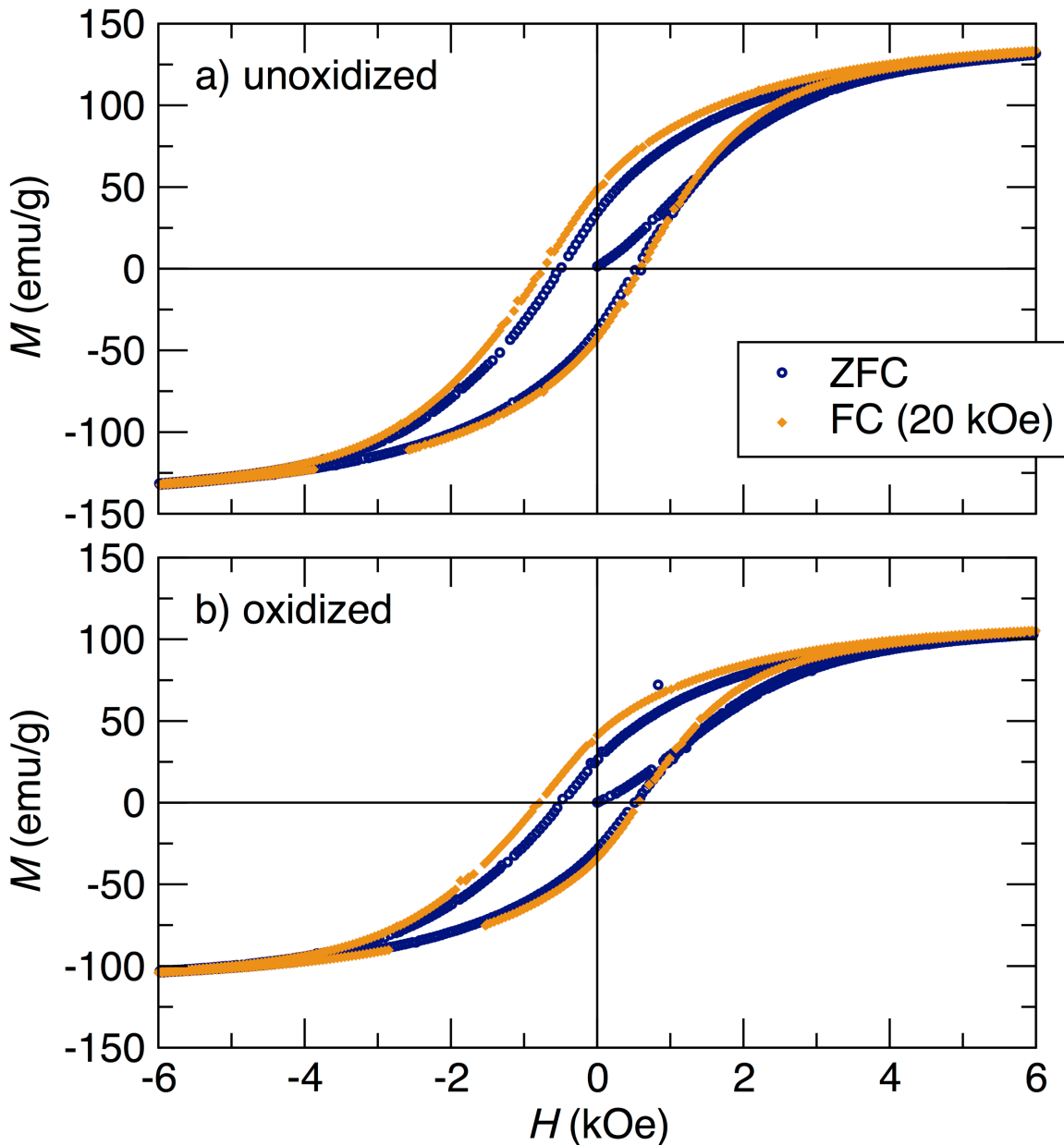

Figure 5: Magnetic hysteresis loops of Fe_3N nanoparticles measured at 2 K. For both the pristine nanoparticles (a) and the oxidized core-shell nanoparticles (b), there is a shifting and broadening of the hysteresis loops when the sample is

field cooled (H = 2 kOe) *vs.* when it is cooled in no field. The observed exchange field (amount of shifting) is H_E = 220 Oe for (a) and H_E = 300 Oe for (b).

When annealed to only 473 K instead of 573 K, the synthesis product exhibited an X-ray diffraction pattern similar to what has been described for ε-Fe_2N (Figure 8 (b)).[47] The structure of ε-Fe_2N is similar to the structure of ε-Fe_3N but with disordered nitrogen vacancies. According to TEM, the sample has crystalline and amorphous parts, and the particle size is 15.1 (± 8.0) nm, determined by measuring 38 particles. Its Fe:N ratio is 2:1, according to EDS. Diffraction contrast TEM images are shown in Figure 6 for a representative Fe_2N agglomerate (Figure 6 (a)). Figure 6 (c) shows a selected area electron diffraction pattern acquired from the area indicated in Figure 6 (a). The most prominent diffraction rings were indexed using the ε-Fe_2N structure.[47] One recognizes that around the diffraction spots there is also a ring structure being overlaid indicating an amorphous sample part. This amorphous part shows that the crystallization process is not yet finished at this temperature. The Fe_2N shows reduced magnetism compared to the Fe_3N particles (16 emu/g vs 106 emu/g at 300 K) due in part to a lower concentration of Fe and in part to a lower moment on each Fe atom (1.1 μ_B/Fe *vs.* 0.37 μ_B/Fe) (Figure 7).
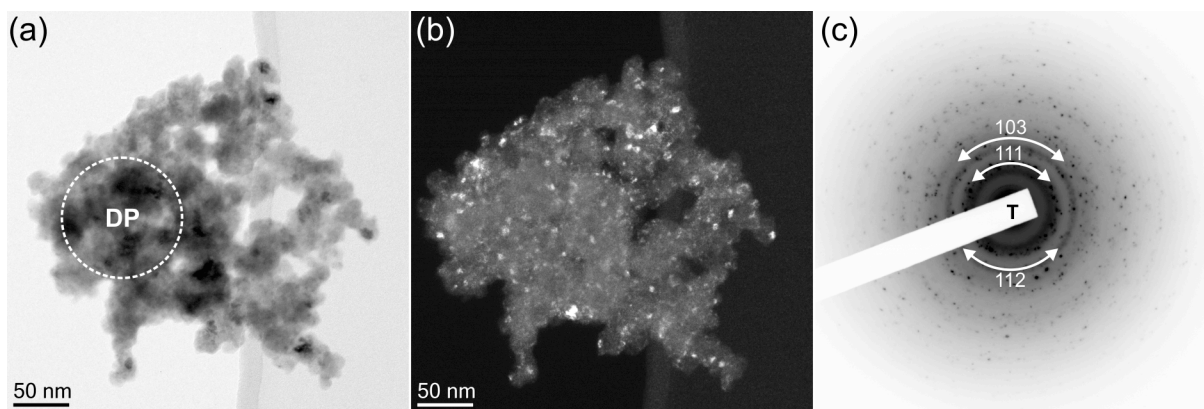

Figure 6: Diffraction contrast TEM images of a representative Fe_2N agglomerate annealed at 473 K: (a) bright-field and (b) dark-field. (c) Selected area diffraction pattern indexed according to the structure model of Fe_2N.[47]
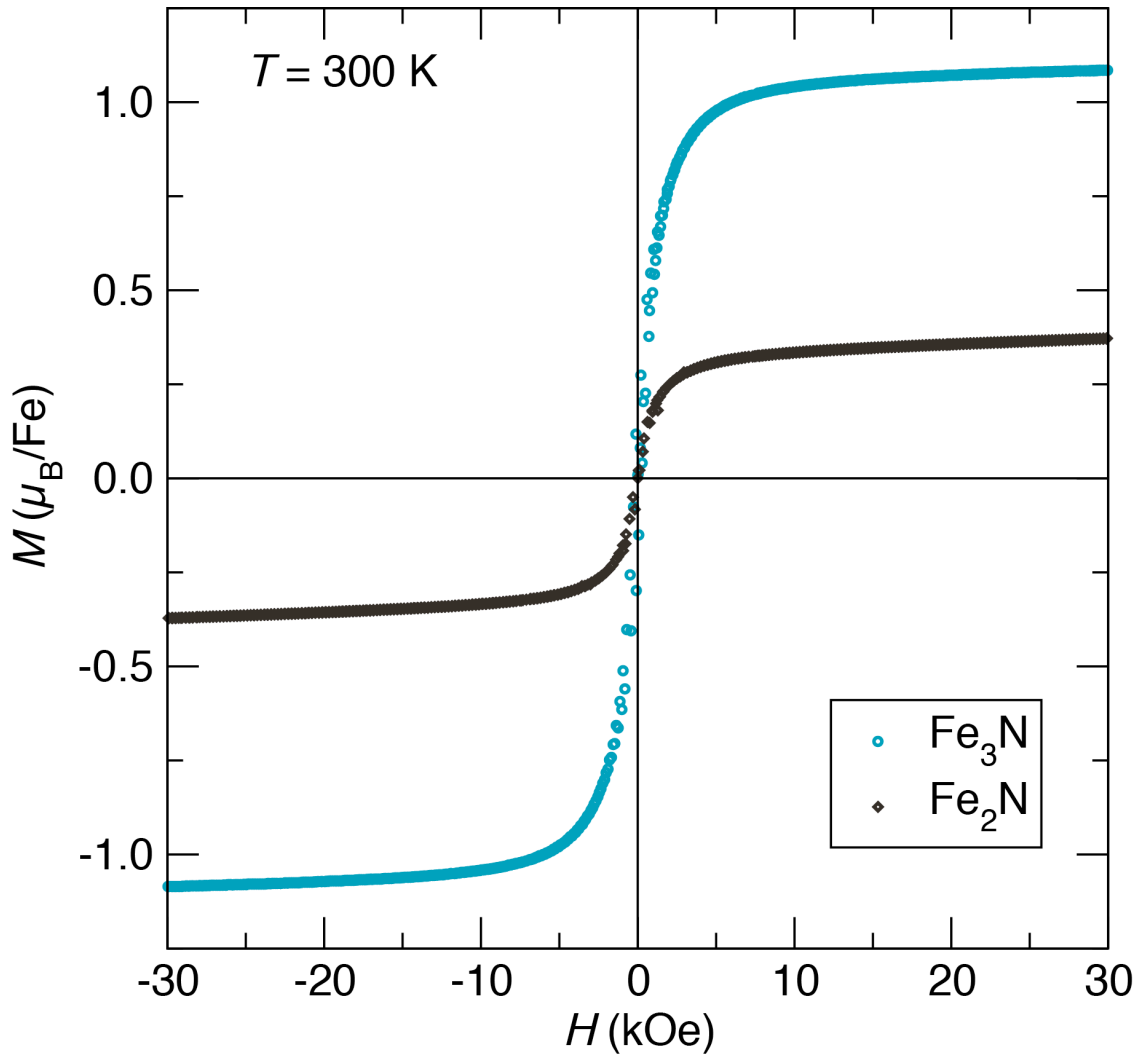
Figure 7: Comparison of the room-temperature magnetization of the ε-Fe$_3$N (annealed at 573 K) and ε-Fe$_2$N (annealed at 473 K) particles. The ε-Fe$_2$N particles show much lower average moment per Fe atom than the ε-Fe$_3$N particles (1.1 μ_B/Fe *vs.* 0.37 μ_B/Fe).

Changes that occur upon annealing were analyzed by a step-wise X-ray diffraction investigation (Figure 8). The as-prepared sample (Figure 8 (a)) shows broad Bragg reflections that appear at 2θ positions matching those of FeN with NaCl-type structure. This is confirmed by electron diffraction (supporting information). Then, as described above, ε-Fe_2N and ε-Fe_3N is formed below 473 K (Figure 8 (b)) and 573 K (Figure 8 (c)), respectively. Rietveld refinement of the X-ray diffraction measurements can be used to estimate the nitrogen content of the ε-Fe_3N_{1+x} phases.[48] After annealing at 473 K and 573 K, the composition as determined by Rietveld refinement is close to the boundary phases ε-Fe_2N and ε-Fe_3N, respectively.

At higher temperatures, decomposition of the iron nitride was observed. After annealing at 673 K, a mixture of ε-Fe_3N, γ'-Fe_4N and α-Fe was detected (Figure 8 (d)). Raising the temperature to 773 K or even 873 K resulted in single-phase α-Fe. However, the reflections of the sample that was annealed at 773 K were slightly shifted to smaller 2θ values as compared to the sample that was annealed at 873 K. This indicates the presence of interstitial nitrogen in the α-Fe below the detection limit of the EDS detector.
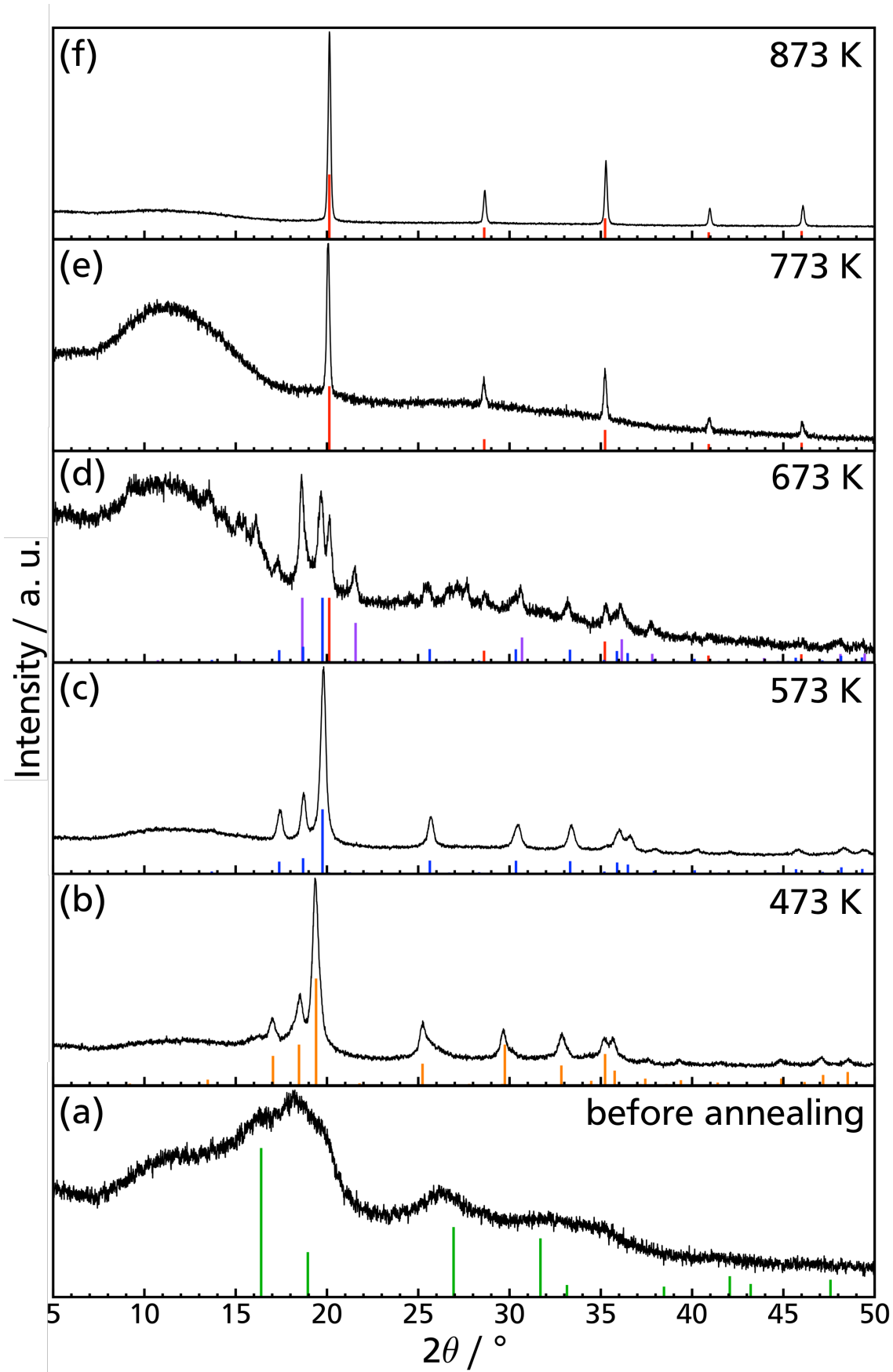
Figure 8: X-ray powder diffraction of the sample (a) before annealing and after annealing at (b) 473 K, (c) 573 K, (d) 673 K, (e) 773 K, (f) 873 K compared to literature data of FeN (green, #41258),[49] ε-Fe$_2$N (orange, #24651),[47] ε-Fe$_3$N (blue, #79984),[50] α-Fe (red, #191830)[51] and γ'-Fe$_4$N (purple, #79980).[50]

Conclusions

Nanoscale transition metal nitrides like ε-Fe$_3$N (as well as ε-Fe$_2$N and FeN) can be produced using the method presented here, thus opening the way to oxygen and carbon-free samples that allow for magnetic characterization of the pure compounds. Compared to the liquid ammonia synthesis route, traditional solid-gas reactions led to oxygen or carbon-containing or multi-phase products with larger size distributions of the particles. Magnetization as a function of temperature up to temperatures above T_C is reported for the first time on ε-Fe$_3$N nanoparticles. Partial oxidation of the pristine Fe$_3$N particles resulted in Fe$_3$N-Fe$_x$O$_y$ core-shell nanoparticles, as shown by EELS mappings. Upon cooling in a magnetic field, the nanoparticles of Fe$_3$N showed shifted and broadened hysteresis loops, both for the unoxidized and oxidized particles. In previous studies of ε-Fe$_3$N particles, the particles always contained iron oxide and this shifting was attributed to exchange bias between the ferromagnetic Fe$_3$N and antiferromagnetic iron oxide. This new synthetic preparation allowed for the observation of asymmetric hysteresis in oxygen-free particles, suggesting that surface disorder, rather than an antiferromagnetic-ferromagnetic interface, is responsible for the behavior.

Supporting information available: Transmission electron microscopy of the iron nitride particles before annealing, study of the crystallization of iron nitride during electron irradiation, transmission electron microscopy after annealing at 773 K, temperature programs used for annealing, particle size distributions after annealing at 573 K and 773 K, X-ray diffraction of ε-Fe$_3$N after Rietveld refinement, estimation of nitrogen concentration after annealing at 473 K and 573 K.

REFERENCES

(1) Kurian, S.; Gajbhiye N. S. Low temperature and in-field Mössbauer spectroscopic studies of ε-Fe$_3$N particles synthesized from iron–citrate complex. *Chem. Phys. Lett.* **2010**, *493*, 299-303.

(2) Takahashi, T.; Burghaus, J.; Music, D.; Dronskowski, R.; Schneider, J. M. Elastic properties of γ'-Fe$_4$N probed by nanoindentation and ab initio calculation. *Acta Mater.* **2012**, *60*, 2054-2060.

(3) Coey, J. M. D.; Smith, P. A. I. Magnetic nitrides. *J. Magn. Magn. Mater.* **1999**, *200*, 405-424.

(4) Kim, T. K.; Takahashi, M. New Magnetic Material Having Ultrahigh Magnetic Moment. *Appl. Phys. Lett.* **1972**, *20*, 492-494.

(5) Suzuki, S.; Sakumoto, H.; Minegishi, J.; Omote, Y. Coercivity and Unit Particle Size of Metal Pigment. *IEEE Trans. Magn.* **1981**, *17*, 3017-3019.

(6) Matar, S. F.; Demazeau, G.; Siberchicot, B. Magnetic Particles derived from Iron Nitride. *IEEE Trans. Magn.* **1990**, *26*, 60-62.

(7) Kramm, U. I.; Herranz, J.; Larouche, N.; Arruda, T. M.; Lefevre, M.; Jaouen, F.; Bogdanoff, P.; Fiechter, S.; Abs-Wurmbach, I.; Mukerjee, S.; Dodelet, J. P. Structure of the catalytic sites in Fe/N/C-catalysts for O$_2$-reduction in PEM fuel cells. *Phys. Chem. Chem. Phys.* **2012**, *14*, 11673-11688.

(8) Namiki, Y.; Matsunuma, S.; Inoue, T.; Koido, S.; Tsubota, A.; Kuse, Y.; Tada, N. Magnetic Nanostructures for Biomedical Applications: An Iron Nitride Crystal/Cationic Lipid Nanocomposite for Enhanced Magnetically Guided RNA Interference in Cancer Cells. In *Nanocrystal*, Masuda, Y., Ed.; InTech: Rijeka, 2011; Chapter 13, 349-372.

(9) Bhattacharyya, S. Iron Nitride Family at Reduced Dimensions: A Review of Their Synthesis Protocols and Structural and Magnetic Properties. *J. Phys. Chem. C* **2015**, *119*, 1601-1622.

(10) Yamaguchi, K.; Yui, T.; Yamaki, K.; Kakeya, I.; Kadowaki, K.; Suemasu, T. Epitaxial growth of ferromagnetic Fe_3N films on Si(111) substrates by molecular beam epitaxy. *J. Cryst. Growth* **2007**, *301-302*, 597-601.

(11) Dirba, I.; Schwöbel, C. A.; Diop, L. V. B.; Duerrschnabel, M.; Molina-Luna, L.; Hofmann, K.; Komissinskiy, P.; Kleebe, H.-J.; Gutfleisch, O. Synthesis, morphology, thermal stability and magnetic properties of α''-$Fe_{16}N_2$ nanoparticles obtained by hydrogen reduction of γ-Fe_2O_3 and subsequent nitrogenation. *Acta Mater.* **2017**, *123*, 214-222.

(12) Mi, W. B.; Guo, Z. B.; Feng, X. P.; Bai, H. L. Reactively sputtered epitaxial γ'-Fe_4N films: Surface morphology, microstructure, magnetic and electrical transport properties. *Acta Mater.* **2013**, *61*, 6387-6395.

(13) Dirba, I.; Komissinskiy, P.; Gutfleisch, O.; Alff, L. Increased magnetic moment induced by lattice expansion from α-Fe to α'-Fe_8N. *J. Appl. Phys.* **2015**, *117*, 173911.

(14) Nicholls, D. *Topics in Inorganic and General Chemistry, Monograph 17: Inorganic Chemistry in Liquid Ammonia*; Elsevier Scientific Publishing Company: Amsterdam, 1979.

(15) Lagowski, J. J. Liquid Ammonia. *Synth. React. Inorg., Met.-Org., Nano-Met. Chem.* **2007**, *37*, 115-153.

(16) Thompson, J. C. Electrons in Liquid Ammonia; Oxford University Press: Oxford, 1976.

(17) Moore, T. E.; Watt, G. W. Reactions of Cobalt(III), Cobalt(II), and Iron(II) Oxides in Liquid Ammonia. *J. Am. Chem. Soc.* **1942**, *64*, 2772-2775.

(18) Watt, G. W.; Jenkins, W. A. The Action of Liquid Ammonia Solutions of Potassium and Potassium Amide upon Iron(II) Bromide. *J. Am. Chem. Soc.* **1951**, *73*, 3275-3276.

(19) Watt, G. W.; Keenan, C. W. The Reduction of Certain Cobalt Salts in Liquid Ammonia. *J. Am. Chem. Soc.* **1952**, *74*, 2048-2050.

(20) Watt, G. W.; Thompson, R. J. The Reduction of Iodopentamminecobalt(III) Iodide and Potassium Hexacyanocobaltate(III) with Potassium in Liquid Ammonia. *J. Inorg. Nucl. Chem.* **1959**, *9*, 311-314.

(21) Gyger, F.; Bockstaller, P.; Gerthsen, D.; Feldmann, C. Ammonia-in-Oil-Microemulsions and Their Application. *Angew. Chem. Int. Ed.* **2013**, *52*, 12443-12447.

(22) Schöttle, C.; Bockstaller, P.; Gerthsen, D.; Feldmann, C. Tungsten nanoparticles from liquid-ammonia-based synthesis. *Chem. Commun.* **2014**, *50*, 4547-4550.

(23) Novikov, V. P.; Pan'kov, V. V.; Kunitskii, L. I. Preparation of Nickel, Iron, and Cobalt Nanopowders via Reduction of Salts with Sodium Dissolved in Liquid Ammonia. *Inorg. Mater.* **2004**, 40, 809-814.

(24) a) Yuan, B.; Yang, M.; Zhu, H. Titanium nitride nanopowders produced via sodium reduction in liquid ammonia. *J. Mater. Res.* **2009**, 24, 448-451; b) Zieschang, A.-M.; Reduktion von Metallsalzen in flüssigem Ammoniak. Master Thesis, TU Darmstadt, August **2015**. c) Zieschang, A.-M., Klemenz, S., Albert, B.; Reduction of metal salts in liquid ammonia. GDCh-Wissenschaftsforum, Dresden, **2015**.

(25) Nogués, J.; Sort, J.; Langlais, V.; Skumryev, V.; Suriñach, S.; Muñoz, J. S.; Baró, M. D. Exchange-bias in nanostructures. *Phys. Rep.* **2005**, *422*, 65-117.

(26) Mitchell, D. R. G. DiffTools: Electron diffraction software tools for Digital Micrograph[TM]. *Microsc. Res. Tech.* **2008**, *71*, 588-593.

(27) Stadelmann, P. A. EMS – a software package for electron diffraction analysis and HREM image simulation in materials science. *Ultramicroscopy* **1987**, *21*, 131-145.

(28) Hendricks, S. B.; Kosting, P. R. The crystal structure of Fe_2P, Fe_2N, Fe_3N and FeB. *Z. Kristallogr. Kristallgeom. Kristallphys. Kristallchem.* **1930**, *74*, 511-533.

(29) Peng, L. M.; Ren, G.; Dudarev, S. L.; Whelan, M. J. Robust Parameterization of Elastic and Absorptive Electron Atomic Scattering Factors. *Acta Crystallogr. A* **1996**, *52*, 257-276.

(30) Watanabe, M.; Okunishi, E.; Ishizuka, K. Analysis of Spectrum-Imaging Datasets in Atomic-Resolution Electron Microscopy. *Microsc. Anal.* **2009**, *23*, 5-7.

(31) Lichtert, S.; Verbeeck, J. Statistical consequences of applying a PCA noise filter on EELS spectrum images, *Ultramicroscopy* **2013**, *125*, 35–42.

(32) Program TOPAS 4.2, Bruker AXS: Karlsruhe, Germany, **2009**.

(33) Robbins, M.; White, J. G. Magnetic Properties of Epsilon-Iron Nitride. *J. Phys. Chem. Solids* **1964**, *25*, 717-720.

(34) Leineweber, A.; Jacobs, H.; Hüning, F.; Lueken, H.; Schilder, H.; Kockelmann, W. ε-Fe_3N: magnetic structure, magnetization and temperature dependent disorder of nitrogen. *J. Alloys Compd.* **1999**, *288*, 79-87.

(35) Niewa, R.; Rau, D.; Wosylus, A.; Meier, K.; Hanfland, M.; Wessel, M.; Dronskowski, R.; Dzivenko, D. A.; Riedel, R.; Schwarz, U. High-Pressure, High-Temperature Single-Crystal Growth, Ab initio Electronic Structure Calculations, and Equation of State of ε-Fe_3N_{1+x}. *Chem. Mater.* **2009**, *21*, 392-398.

(36) Eck, B.; Dronskowski, R.; Takahashi, M.; Kikkawa, S. Theoretical calculations on the structures, electronic and magnetic properties of binary 3d transition metal nitrides. *J. Mater. Chem.* **1999**, *9*, 1527-1537.

(37) Zhang, W. H.; Lv, Z. Q.; Shi, Z. P.; Sun, S. H.; Wang, Z. H.; Fu, W. T. Electronic magnetic and elastic properties of ε-phases $Fe_3X(X=B, C, N)$ from density-functional theory calculations. *J. Magn. Magn.* **2012**, *324*, 2271-2276.

(38) Zhang, P.; Wang, X.; Wang, W.; Lei, X.; Yang, H. Magnetic and hydrazine-decomposition catalytic properties of ε-Fe_3N synthesized from a novel precursor. *J. Mater. Chem. A* **2015**, *3*, 6464-6469.

(39) Schlosser, W. F. The temperature dependence of the magnetic moment of iron, nickel and invar for $T/T_c < 0.5$. *Phys. Lett.* **1972**, *40A*, 195-196.

(40) Ahn, C. C. *Transmission Electron Energy Loss Spectrometry in Materials Science and The EELS Atlas*, Second Edition; Wiley-VCH Verlag GmbH & Co. KGaA: Weinheim, 2004.

(41) Colliex, C.; Manoubi, T.; Ortiz, C. Electron energy-loss-spectroscopy near-edge fine structures in the iron oxygen system, *Phys. Rev. B* **1991**, *44*, 11402-11411.

(42) Calvert C. C.; Brown, A.; Brydson, R. Determination of the local chemistry of iron in inorganic and organic materials, *J. Electron. Spectrosc. Relat. Phenom.* **2005**, *143*, 173-187.

(43) Li, D.; Choi, C. J.; Yu, J. H.; Kim, B. K.; Zhang, Z. D. Nanocrystalline α-Fe and ε-Fe$_3$N particles prepared by chemical vapor condensation process. *J. Magn. Magn. Mater.* **2004**, *283*, 8-15.

(44) Li, D.; Zhang, Z. D.; Li, W. F.; Feng, W. J.; Choi, C. J.; Kim, B. K. Electrical and magnetic properties of ε-Fe$_3$N nanoparticles synthesized by chemical vapor condensation process. *J. Magn. Magn. Mater.* **2006**, *285*, 128-133.

(45) Shoemaker, D. P.; Rodriguez, E. E.; Seshadri, R.; Abumohor, I. S.; Proffen, T. Intrinsic exchange-bias in Zn$_x$Mn$_{3-x}$O$_4$ (x$\leq$1) solid solutions. *Phys. Rev. B* **2009**, *80*, 144422.

(46) Douglas, J. E.; Levin, E. E.; Pollock, T. M.; Castillo, J. C.; Adler, P.; Felser, C.; Krämer, S.; Page, K. L.; Seshadri, R. Magnetic hardening and antiferromagnetic/ferromagnetic phase coexistence in Mn$_{1-x}$Fe$_x$Ru$_2$Sn Heusler solid solutions. *Phys. Rev. B* **2016**, *94*, 094412.

(47) Jack, K. H., The Iron-Nitrogen System: The Crystal Structures of ε-Phase Iron Nitrides. *Acta Crystallogr.* **1952**, *5*, 404-411.

(48) Liapina, T.; Leineweber, A.; Mittemeijer, E. J.; Kockelmann, W. The lattice parameters of ε-iron nitrides: lattice strains due to a varying degree of nitrogen ordering. *Acta Mater.* **2004**, *52*, 173-180.

(49) Suzuki, K.; Morita, H.; Kaneko, T.; Yoshida, H.; Fijimori, H. Crystal structure and magnetic properties of the compound FeN. *J. Alloys Compd.* **1993**, *201*, 11-16.

(50) Jacobs, H.; Rechenbach, D.; Zachwieja, U. Structure determination of γ'-Fe$_4$N and ε-Fe$_3$N. *J. Alloys Compd.* **1995**, *227*, 10-17.

(51) Jing, C., Cao, S. X.; Zhang, J. C. Lattice constant dependence of magnetic properties in bcc and fcc Fe$_x$Mn$_{1-x}$ alloys. *Phys. Rev. B* **2003**, *68*, 224407.

AUTHOR INFORMATION

Corresponding Authors

*[1] Prof. Dr. Barbara Albert, Technische Universität Darmstadt, Eduard-Zintl-Institute of Inorganic and Physical Chemistry, Alarich-Weiss-Str. 12, 64287 Darmstadt, Germany, albert@ac.chemie.tu-darmstadt.de

*[2] Prof. Dr. Ram Seshadri, University of California, Santa Barbara, Department of Chemistry & Biochemistry, Materials Department, and Materials Research Laboratory, University of California, Santa Barbara CA 93106, U.S.A., seshadri@mrl.ucsb.edu

ACKNOWLEDGEMENT